

Application of electron tomography for comprehensive determination of III-V interface properties

Lars Nicolai^{*}, Klaus Biermann, Achim Trampert

Paul-Drude-Institut für Festkörperelektronik, Leibniz-Institut im Forschungsverbund Berlin e.V., Hausvogteiplatz 5-7, 10117, Berlin, Germany

ARTICLE INFO

Keywords:

Electron tomography
Interface
Roughness
Interface width
Correlation length
III-V semiconductor

ABSTRACT

We present an electron tomography method for the comprehensive characterization of buried III-V semiconductor interfaces that is based on chemical-sensitive high-angle annular dark-field scanning transmission electron microscopy. For this purpose, an (Al,Ga)As/GaAs multi-layer system grown by molecular beam epitaxy is used as a case study. Isoconcentration surfaces are exploited to obtain topographic height maps of 120 nm × 120 nm area, revealing the interface morphology. By applying the height-height correlation function, we are able to determine important interface properties like root mean square roughness and lateral correlation length of various interfaces of the (Al,Ga)As/GaAs system characterized by different Al concentrations. Height-difference maps based on isosurfaces corresponding to 30% and 70% of the total compositional difference at the interfaces are used to create topographic maps of the interface width and to calculate an average interface width. This methodology proves differences in the properties of direct and inverted interfaces and allows the observation of interfacial anisotropies.

1. Introduction

Most modern III-V heterostructure devices require a high level of control over the quality of their interfaces due to the large impact on many physical properties like, for example, the electron mobility in quantum wells [1] or the tunneling behavior in sophisticated heterostructures such as quantum cascade lasers [2]. For this reason, an extensive analysis is necessary to understand the relation between structure and functionality of interfaces more precisely [3] and thus enable the development of novel semiconductor devices [4].

In general, planar semiconductor heterostructure interfaces are characterized by two fundamental properties: the morphological roughness and the chemical disorder or intermixing. These properties are typically described by the root mean square (RMS) value of the roughness and the lateral and vertical correlation lengths as well as the interface broadening, i.e., the chemical width of the interface [2,5]. Experimental tools to measure these quantities in the case of buried interfaces are fairly limited. On the one hand, x-ray scattering methods are able to deliver detailed information about surfaces and interfaces on a large scale with low spatial resolution [6], and, on the other hand, spatially resolved methods like cross-sectional scanning tunneling microscopy are used to observe local variations providing, however,

two-dimensional (2D) images [7]. Conventional transmission electron microscopy (TEM) allows to investigate interfaces in cross-sectional samples down to the atomic limit [8]. Additionally, site-specific TEM investigations are made possible by using a focused ion-beam (FIB) preparation technique. TEM images are projections of the illuminated sample, which inherently provide only partial information, which is sometimes erroneous due to the missing depth information [9]. This fact makes it generally challenging to investigate interfaces with roughness variations on the length scale smaller than the foil thickness or to extract any anisotropy.

Semiconductor interfaces must be considered as three-dimensional (3D) objects since almost no real interface is atomically smooth and chemically abrupt [5]. Consequently, tomographic methods should be most appropriate to comprehensively characterize the 3D interface property with respect to roughness and chemical intermixing. Nevertheless, there are very few studies on the tomography of semiconductor interfaces in the literature. Most remarkable are the works on interfaces in Si/SiGe multi-layer structures which are based on atom probe tomography combined with scanning (S)TEM observations [2,10,11]. These studies present quantitative results on interface profiles and the 3D roughness, including data on the lateral and vertical correlation lengths at several successive interfaces. In the case of electron

^{*} Corresponding author.

E-mail address: lars@nicolai-germany.de (L. Nicolai).

tomography at planar buried interfaces, the situation appears even more rudimentary. Here, only investigations of $\text{ZrO}_2/\text{In}_2\text{O}_3$ interfaces by energy-filtered TEM [12] or the study of SiO_2/W interfaces based on annular dark-field (ADF) STEM are available [13]. The latter work suggests how chemically sensitive ADF STEM images can be used for tomographic reconstruction of a III-V semiconductor heterostructure to extensively characterize buried III-V interfaces.

In this contribution, an electron tomography method is developed that allows differentiating between the morphological roughness and the chemical intermixing of III-V semiconductor interfaces by evaluating isoconcentration-surfaces in 3D space. The method enables a quantitative and spatially resolved analysis of important interface parameters like the root mean square (RMS) roughness value σ_{RMS} , the lateral correlation length Λ , or the interface width W .

2. Material and methods

2.1. Sample growth and structure

A well-established $\text{Al}_x\text{Ga}_{1-x}\text{As}/\text{GaAs}$ multi-layer structure is used for this case study to demonstrate the applicability of electron tomography for the comprehensive characterization of a compound semiconductor interface. The sample was intentionally grown for the TEM investigation by molecular beam epitaxy on a GaAs (001) substrate. After the deposition of a 200 nm thick GaAs buffer layer, a short-period superlattice with alternating GaAs/ $\text{Al}_{0.25}\text{Ga}_{0.75}\text{As}$ layers was grown for calibration purposes. Then, the actual structure to be investigated by electron tomography was grown consisting of alternating 50 nm thick $\text{Al}_x\text{Ga}_{1-x}\text{As}$ and 25 nm thick GaAs layers, whereby the Al content was increased in steps of $x = 25\%$ for the first three $\text{Al}_x\text{Ga}_{1-x}\text{As}$ layers and for the rest increased in steps of 5% until pure AlAs was reached. The substrate temperature was fixed at 600 °C, the V/III beam equivalent pressure ratio at about 20, and the growth rate was 0.15 nm/s for all the layers. As a result, a multi-layer structure has been manufactured that provides various coherent interfaces as ideal objects for the tomography study.

A cross-sectional view of the complete microstructure is depicted in Fig. 1a by showing a high-angle (HA)ADF STEM micrograph of a cross-sectional lamella prepared by FIB. Using the HAADF imaging conditions leads to the formation of a chemical-sensitive signal where the measured intensity is proportional to the thickness as well as the atomic number of atoms (Z-contrast) in the sample [14]. The HAADF STEM micrograph demonstrates the increase in contrast for the various (Al,Ga)As layers from bottom to top in accordance with the nominal concentration

variation of the layers indicated by the schematic on the left in Fig. 1a. On a closer inspection, the STEM micrograph already reveals the presence of a morphological roughness in the upper two GaAs-on-(Al,Ga)As interfaces. In addition, an atomically resolved HAADF micrograph and the corresponding intensity line profile of the interface, which is labeled with a red arrow, are indicated in Fig. 1b and c, respectively. They show that the interface has a rather large measured width of $W = (5.3 \pm 0.3)$ nm applying for the evaluation the 10%-to-90%-criterion and a sigmoidal fit which is commonly used to describe the profile of III-V semiconductor interfaces [15]:

$$I(x) = I_0 / \left[1 + \exp\left(\frac{-x}{L}\right) \right] \quad (1)$$

where $L = W/4.39$ is a parameter for the interface width and I_0 is the change in intensity corresponding to the change in the composition of $\text{Al}_x\text{Ga}_{1-x}\text{As}$ across the interface. The present large interface width, together with the observed lateral roughness, distinguishes this sample ideally as a case study.

2.2. Specimen preparation

For the electron tomography investigation, needle-shaped specimens were prepared out of the compact multi-layer system with the needle axis perpendicular to the surface by applying the site-specific FIB preparation technique. For that purpose, a Jeol JIB-4501 dual-beam (electron- and gallium-beam) microscope was used to perform a standard lift-out technique [16] with additional thinning steps to obtain a needle-shaped specimen with a diameter of ca. 250 nm [17–19]. The result of the final needle is shown in Fig. 2a.

The selected diameter of the tomography needle is a compromise between achieving electron transparency and having a large probe volume which, on the one hand, can be reconstructed and further analyzed. On the other hand, the sample has to fulfill the projection requirement for electron tomography, i.e., the intensity should be a monotonic function of the physical property to be measured [20]. In addition, a linear relationship would allow to quantitatively correlate the intensity with the chemistry of the sample for a known thickness and prevents non-linear effects like the cupping artifact [21]. With this in mind, a wedge-shaped specimen of the same material was prepared using FIB to verify the linear relationship. Fig. 2b shows two line profiles of the HAADF intensity across the wedge-shaped specimen with the related HAADF micrograph given in the inset. The black line profile corresponds to a GaAs layer and the red to the $\text{Al}_{0.95}\text{Ga}_{0.05}\text{As}$ layer. The

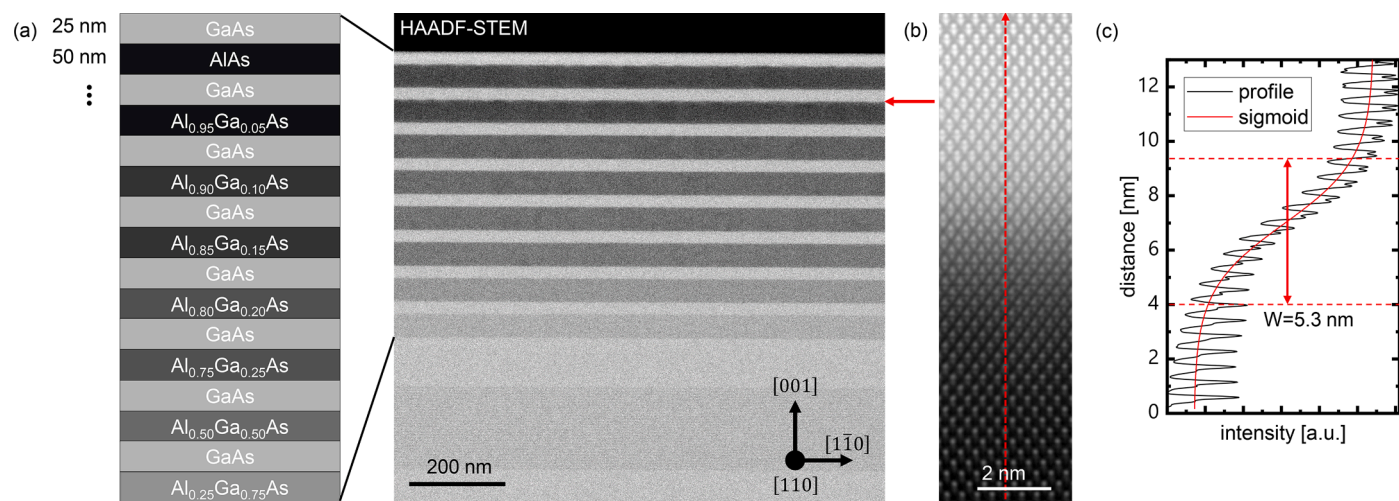


Fig. 1. (a) HAADF STEM micrograph of a FIB lamella of the multi-layered (Al,Ga)As/GaAs structure and a schematic showing the change of the composition of the $\text{Al}_x\text{Ga}_{1-x}\text{As}$ layers. (b) Atomically resolved HAADF STEM image of interface region marked by a red arrow and (c) corresponding intensity profile and a fit based on the sigmoid function.

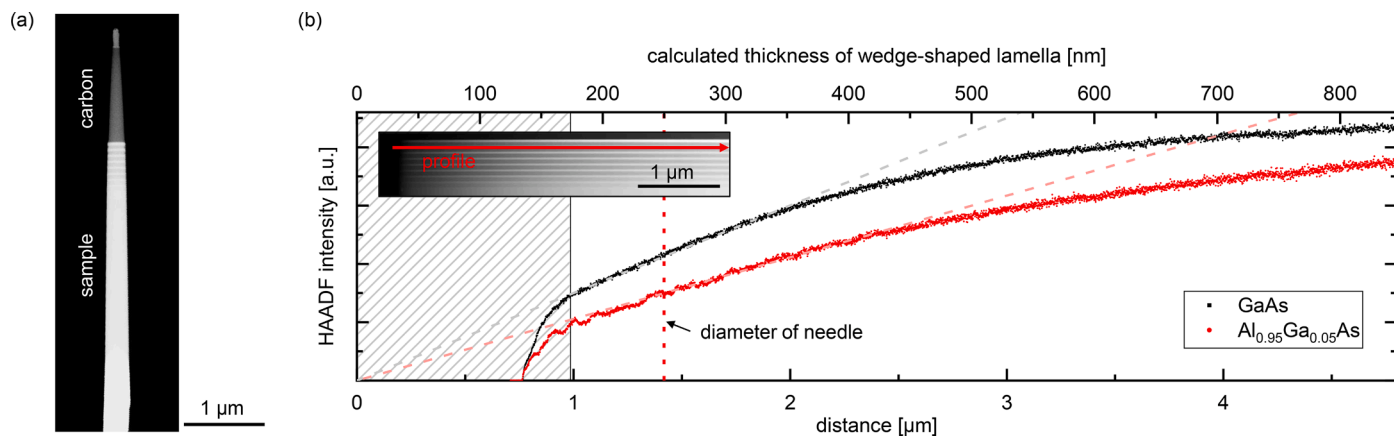


Fig. 2. (a) HAADF STEM image of the tomography needle. (b) Profile of the HAADF intensity across a wedge-shaped lamella for the GaAs and the $\text{Al}_{0.95}\text{Ga}_{0.05}\text{As}$ layer. The upper x-axis shows the calculated thickness of the lamella based on the known angle of the wedge. The thinnest region of the lamella deviates from the perfect wedge-shape and is therefore disregarded (gray striped area). A linear relationship between the HAADF intensity and the sample thickness exists up to a thickness of ca. 350 nm. Therefore, the chosen diameter of the tomography needle (marked by a red dotted line) is within the linear regime.

thickness at each point of the sample could be calculated since the angle of the wedge is known. The dashed lines represent the ideal linear relationship of thickness and intensity. The gray striped area in the graph marks the region where the sample deviates from a perfect wedge-shape (below a calculated thickness of 175 nm), and this area is therefore disregarded. The chosen diameter of the tomography needle of 250 nm is marked as a red dotted line. As can be seen in the figure, the diameter is within the linear regime since the intensities deviate from a linear relationship at higher thicknesses (from ca. 350 nm for GaAs and 450 nm for $\text{Al}_{0.95}\text{Ga}_{0.05}\text{As}$). Needles with a diameter of more than 500 nm would still allow obtaining a useful reconstruction for qualitative analysis. Still, the exact relationship between intensity and composition would be violated, which is essential for the following interface analysis [22]. It must be mentioned that the intensity-thickness relationship strongly depends on the chosen camera length and ADF detector, which are, in this case, the same settings as for the tomographic tilt series acquisition (see next paragraph).

Finally, the needle was transferred to a support for a double-tilt tomography holder, the EN-holder from Mel-Build corporation, using a micro-manipulator from Kleindiek Nanotechnik GmbH. The double-tilt feature of this tomography holder allows compensating small deviations of the growth direction to the rotation axis of the goniometer.

2.3. Acquisition of tilt series and reconstruction

The tilt series for electron tomography was acquired using a C_5 -corrected Jeol ARM 200F with an accelerating voltage of 200 kV. The microscope was operated in scanning mode, and the signal was acquired using a bright-field (BF) as well as two ADF detectors. A camera length of 3 cm was chosen to obtain an electron acceptance angle of 80–320 mrad for one of the ADF detectors. All detector signals were recorded, however, only the mentioned HAADF signal of the ADF detector was used for the reconstruction. Due to a higher contrast, the signal of the BF detector was used for the probe tracking of the automatic tilt series acquisition, which was controlled by the STEM recorder software from System In Frontier Inc.

The scanning array has a size of 2048×2048 pixels with a pixel dwell time of 20 μs and a pixel size of 0.33^2 nm^2 . A condenser aperture of 30 μm was inserted to obtain an appropriate focus depth. A tilt series from -85° to $+85^\circ$, which is the maximum possible tilt of the holder, with 2° tilt steps was carried out, leading to a tilt series with a total of 86 micrographs which facilitates only a very small missing wedge effect [20]. The small tilt steps of 2° were used since a larger number of micrographs in the tilt series improves the resolution of the tomogram, which is described by the Crowther criterion [23]. After each

goniometer tilt, the acquisition started with a delay of at least 90 s to reduce the total sample drift during the scanning process. An extract of the tilt series is depicted in Fig. 3a. Complementary selected area diffraction patterns were recorded to correlate the orientation of the crystal with the rotation angles and hence the orientation of the final tomogram. Two of these diffraction patterns are shown as an inset in the figure. They also show the advantage of using a double-tilt tomography holder: The [001] growth direction could be matched with the rotation axis of the goniometer. In this way, every zone axis (ZA) perpendicular to the [001] direction could be reached by only rotating around one axis. Remarkably, the images along the ZA provide a clear contrast between crystalline and amorphous parts of the needle edges (cf., Fig. 3b) indicative for the channeling effect [24,25]. Nevertheless, the effects are small and do not have a significant influence on our analysis.

The IMOD software package [26] was used to manually align the micrographs with high precision so that the central needle axis is also the rotation axis of the Radon transformation. The final tomograms were calculated by simultaneous iterative reconstruction technique (SIRT) algorithm using 60 iterations. For this purpose, the ASTRA toolbox [27, 28] python scripts were implemented into the Amira Avizo software. The latter was used to execute the Python script, visualize the 3D data and extract the isosurfaces. The Avizo software was also utilized for post-processing of the reconstructed data. The 3D non-local mean filter (NLMF) was applied for denoising the tomographic data. The NLMF is a new filter that reduces the noise without affecting fine structures and textures [29]. Additionally, the voxels (3D pixels) were binned to further increase the signal-to-noise ratio. In this case, the voxel volume after binning is 0.66^3 nm^3 . The isosurfaces were transformed into topographic maps and analyzed by the open-source software Gwyddion [30].

3. Results and discussion

3.1. Tomogram of heterostructure

The reconstruction of the complete $\text{Al}_x\text{Ga}_{1-x}\text{As}/\text{GaAs}$ multi-layer system results in a 3D dataset consisting of voxels with different intensities, which are based on the Z-contrast of the original HAADF tilt series. This data set can be visualized in various ways. A typical 3D representation of the reconstructed tomography needle is given in Fig. 4a with a partial cut exposing the interior and revealing the stacking sequence of the various $\text{Al}_x\text{Ga}_{1-x}\text{As}$ (blue and green) and GaAs (red) layers. The outer surface of the tomography needle is modulated due to a preferential sputtering of the $\text{Al}_x\text{Ga}_{1-x}\text{As}$ layers during the FIB preparation process. A 2D slice with a finite thickness of one voxel, i.e., 0.66 nm, is taken from the center of the reconstruction, which reflects the voxel

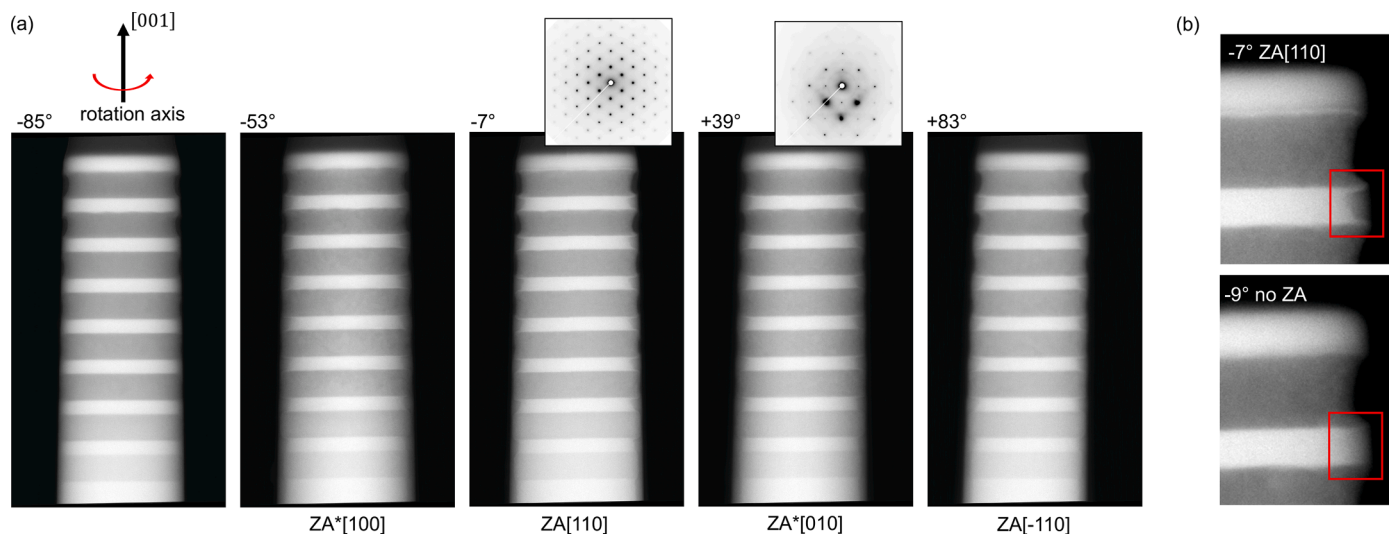


Fig. 3. Extract from the tomographic tilt series. (a) HAADF STEM micrographs at different tilt angles are shown. For two of the tilt angles, diffraction patterns are given, which were used to correlate the tilt angles with the crystal orientation of the specimen. The zone axis (ZA) is given for the micrographs, whereby the asterisked ZAs are not exact since the tilt of these micrographs is off by 1° . (b) Magnified HAADF STEM image of the edge of the tomographic needle taken precisely in the [110] ZA, and another image with a tilt of 2° deviating from this ZA condition. Only in ZA condition, a contrast between crystalline and amorphous GaAs is visible.

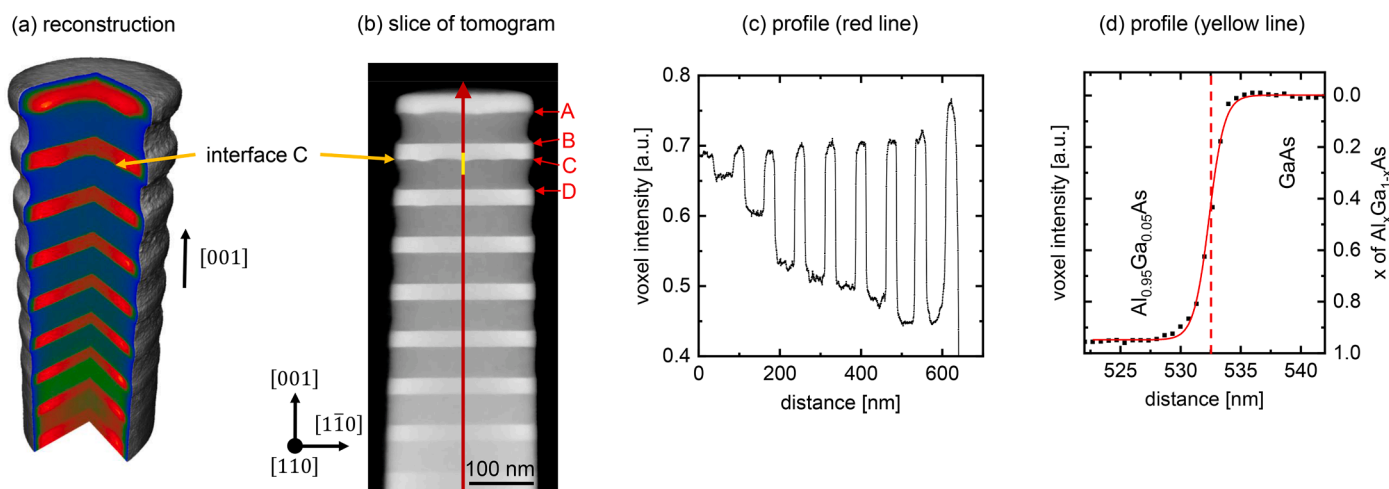


Fig. 4. Reconstruction of the multi-layered $\text{Al}_x\text{Ga}_{1-x}\text{As}/\text{GaAs}$ structure. (a) 3D representation of the tomogram. (b) Slice of the reconstruction revealing the presence of a morphological roughness. (c) Line profile extracted from the center of the reconstruction [cf. the red line in (b)]. (d) Line profile across the center of interface C [cf. yellow line in (b)].

intensity variations across the different layers (cf. Fig. 4b). The layers with high intensity (bright layers) correspond to GaAs due to the higher mean atomic number compared to the $\text{Al}_x\text{Ga}_{1-x}\text{As}$. This slice qualitatively illustrates the presence of a morphological interface roughness, as it is, for example, clearly visible for the interface labeled C. If an intensity profile through the center of the slice vertically across all interfaces is extracted (marked by a red arrow), the changes in voxel intensities are obtained (Fig. 4c). The changes are equivalent to the increase in Al-concentration in the different layers and therefore reflecting the composition of the $\text{Al}_x\text{Ga}_{1-x}\text{As}$ layers. Fig. 4d shows the intensity profile of the single $\text{Al}_{0.95}\text{Ga}_{0.05}\text{As}/\text{GaAs}$ interface. This profile reveals the presence of a chemical width of $W = (2.81 \pm 0.02)$ nm at this interface position. Due to the slice thickness of 0.66 nm, there is obviously no projection problem in this case in contrast to the analysis given in Fig. 1, and the value corresponds to the pure chemical intermixing.

Since the voxel intensities reflect the composition of the sample in 3D space, basically, the interfaces are comprehensively charted. In this sense, slices in varying positions and orientations with any selected

thickness are possible and already allow a simple analysis of the interfaces, subtracting any projection problem. However, extracting line profiles at every position of the many interfaces to evaluate possible fluctuations of the interface position and width would not be feasible. Therefore, in the following, isosurfaces are created to allow a complete qualitative and quantitative analysis of the interface properties. Isosurfaces are surfaces following a constant value of voxel intensity. Due to the direct correspondence between voxel intensity and chemical composition, these isosurfaces are also isoconcentration-surfaces.

3.2. Analysis of the morphological roughness using electron tomography

Fig. 5 summarizes the procedure for creating a topographic height map of the III-V interface. Due to the presence of both, morphological roughness and chemical width, the position of the interface needs to be defined first. It is appropriate to indicate this position at half of the voxel intensity difference between adjacent layers in the tomogram. For this purpose, the mean voxel intensities of the neighboring (Al,Ga)As and

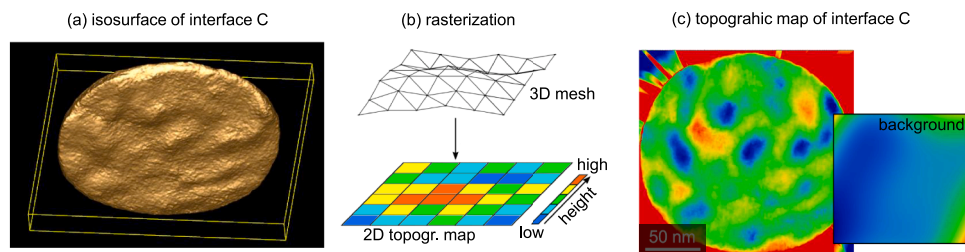


Fig. 5. Creation of topographic maps. (a) Iso-surface at the intermediate voxel intensity of the $\text{Al}_{0.95}\text{Ga}_{0.05}\text{As}/\text{GaAs}$ interface (labeled as interface C). (b) Schematic of the rasterization process used to transform isosurfaces into height maps. (c) Final topographic map for interface C after background subtraction. The subtracted background is shown as an inset.

GaAs layers are exactly determined by histogram formation, and the intermediate intensity of these two mean values was calculated. Subsequently, an isosurface is generated based on this intermediate voxel intensity. As an example, Fig. 5a shows the isosurface for interface C, indicating the presence of a morphological roughness. To allow a quantitative analysis, the isosurface needs to be transformed into a topographic height map using the Gwyddion software package. Therefore, in the next step, the irregular 3D mesh is projected onto a 2D array, as schematically shown in Fig. 5b. Each pixel of this array is thereby reproducing the average height value of the mesh point above. In dense regions, where more vertices fall into one pixel, the height value was averaged, whereas, in sparse locations, where no vertex falls into one pixel, the intensity value was interpolated from close pixels. Using this rasterization, the topographic map is finally obtained and is exemplary given for interface C in Fig. 5c. A background intensity, which is shown as an inset, was subtracted to counteract tilts of the surfaces with regard to the projection plane, avoiding systematic errors during the analysis.

Fig. 6a represents the results of the topographic mapping of the top

four interfaces between AlAs and GaAs (labeled A, B) as well as between $\text{Al}_{0.95}\text{Ga}_{0.05}\text{As}$ and GaAs (labeled C, D, cf. Fig. 4b), visualizing the 2D spatial distribution of the morphological roughness.

Strong differences in the magnitude of the roughness are visible between direct $\text{Al}_x\text{Ga}_{1-x}\text{As}$ -on-GaAs and inverted GaAs-on- $\text{Al}_x\text{Ga}_{1-x}\text{As}$ interfaces, cf. line profile of interface A and B shown in Fig. 6b. Smooth interface structures with height variations in the order of a few Ångstrom are detected for the direct interfaces, whereas the height variations of inverted interfaces are up to more than an order of magnitude higher. For a more precise quantification of the roughness, the root mean square (RMS) value σ_{RMS} is calculated as follows:

$$\sigma_{RMS} = \sqrt{\frac{1}{N} \sum_{n=1}^N (z_n - \bar{z})^2} \quad (2)$$

N is the number of pixels, z_n the height value of the n -th pixel and \bar{z} the average height. RMS values have been determined for each interface over the whole $120 \text{ nm} \times 120 \text{ nm}$ area of the topographic maps with the

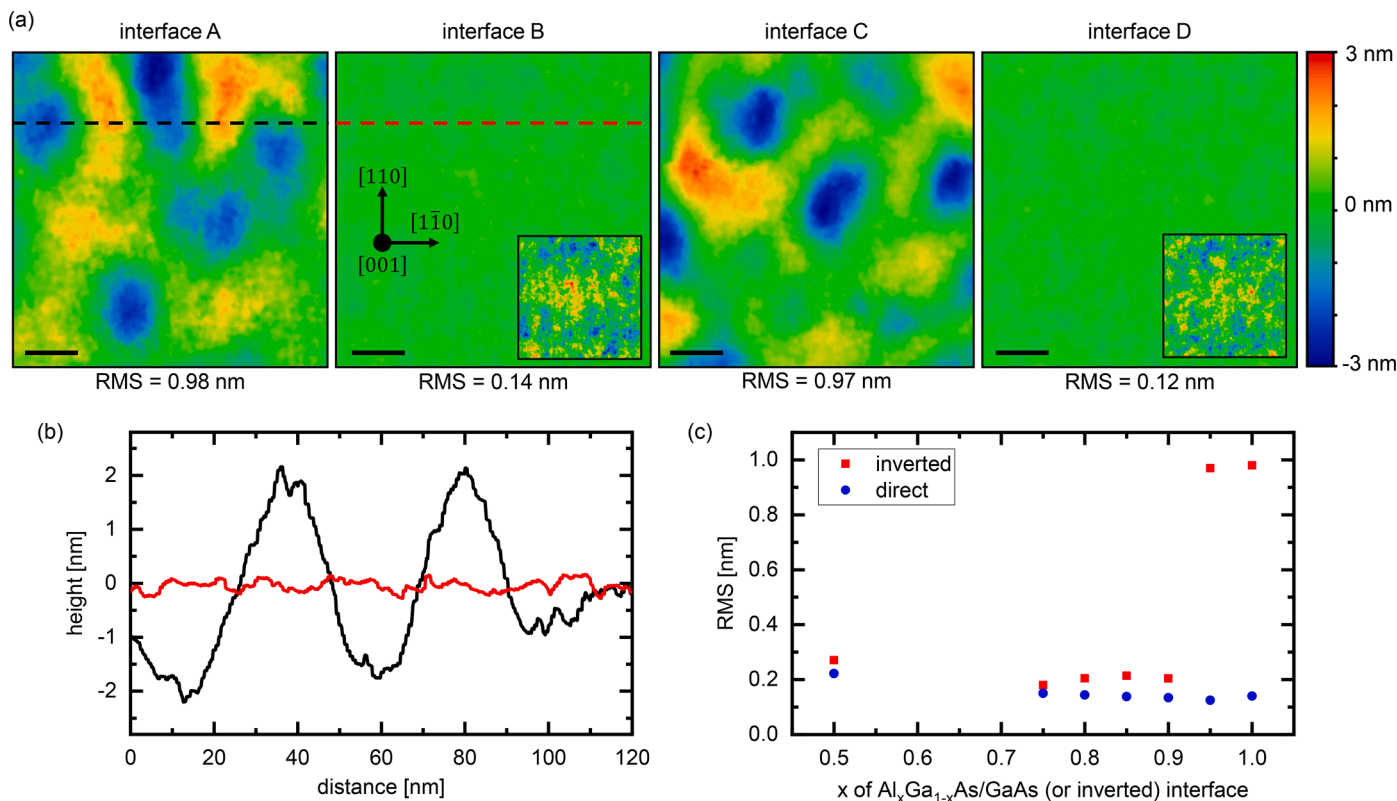


Fig. 6. Analysis of the topographic maps. (a) Topographic maps of the upper four interfaces labeled A, B, C, and D with the root mean square value for each of the interfaces, respectively. The insets for interfaces B and D show the same topographic maps but with a blown-up scaling from -0.5 nm to 0.5 nm . The black scale bar corresponds to 20 nm . (b) Height profile extracted at interface A (black line) and B (red line). (c) Calculated RMS values for all investigated direct and inverted interfaces.

result for the upper four interfaces of 0.98 nm and 0.97 nm for the inverted and 0.14 nm and 0.12 nm for the direct interfaces, respectively. The RMS values for all investigated interfaces are summarized in the graph shown in Fig. 6c.

In agreement with the topographic mapping, the RMS values are always higher for the inverted compared to the direct interfaces with the highest difference at the upper two AlAs/GaAs and Al_{0.95}Ga_{0.05}As/GaAs interfaces. This difference in roughness between direct and inverted (Al, Ga)As/GaAs interfaces has also been observed by others (see, for instance, Ref. [31]).

The error Δz_n for the height values z_n in the topographic maps is estimated by the amplitude of the noise of these maps. The waviness with low frequency is attributed to the roughness of the interface, whereas height fluctuations on a small scale with high frequency are attributed to noise. The amplitude of these fluctuations is about $\Delta z_n = 0.1$ nm. Consequently, the error of a calculated height difference between two positions is about 0.14 nm. The error of the total RMS roughness $\Delta\sigma_{RMS}$ is expected to be lower than the error of a single height difference calculation.

Apart from that, the RMS value is not sufficiently meaningful in order to describe the characteristic lateral length scale defining the average spacings between interfacial steps. The height-height correlation function (HHCF) is used to extract this characteristic length by evaluating the in-plane correlation length, which is defined by the average squared difference in height z of two points separated by distance τ , $H(\tau) = \langle |z(\tau') - z(\tau' + \tau)|^2 \rangle$ [32,33]. The one-dimensional HHCF for discrete pixels is specified as:

$$H_x(\tau_x) = \frac{1}{N(M-m)} \sum_{l=1}^N \sum_{n=1}^{M-m} (z_{n+m,l} - z_{n,l})^2 \quad (3)$$

where $m = \tau_x/\Delta_x$. Δ_x is the discrete sampling interval (pixel size), M is the size of the pixel array in x -direction and N the size in the perpendicular direction. It is well established that the HHCF can be phenomenologically described by [34]:

$$H_x(\tau_x) = 2\sigma_x^2 \left[1 - \exp\left(-\left(\frac{\tau_x}{\Lambda_x}\right)^{2h_x}\right) \right] \quad (4)$$

where σ_x is the one-dimensional RMS value, Λ_x the correlation length and h_x the Hurst parameter. The HHCF function is plotted for the in-

terfaces C and D along the two crystallographic directions $x = [110]$ and $x = [\bar{1}\bar{1}0]$ in Fig. 7a and b, respectively. After fitting the curve according to Eq. (4), the fit parameters reveal a lateral correlation length of (13.3 ± 0.1) nm and (13.7 ± 0.3) for interface C along the $[\bar{1}\bar{1}0]$ and $[110]$ direction, and (3.77 ± 0.04) nm and (6.9 ± 0.1) nm for interface D along the $[\bar{1}\bar{1}0]$ and $[110]$ direction, respectively. These fit parameters for all interfaces along both directions are summarized in Fig. 7c and d, respectively. The evaluation of the retrieved data shows that a consideration of all parameters describing the interface is necessary since they do not have to be correlated. The one-dimensional roughness σ_x agrees well with the previously determined RMS values σ_{RMS} and shows no indication of anisotropy since the values along the $[110]$ and $[\bar{1}\bar{1}0]$ direction are very similar to each other. In contrast, the correlation length Λ_x of the direct interfaces is systematically higher along the $[\bar{1}\bar{1}0]$ direction compared to $[110]$ direction, whereas in the case of the inverted interface, this anisotropy is not detectable. Due to the higher roughness values of the inverted interface, such anisotropy can smear out, or the measured area of the tomogram is not large enough to detect it. The direct interface with its very low roughness rather shows the known property of a step-terrace system and thus an anisotropy along the different crystallographic $\langle 110 \rangle$ directions. Taking these interface parameters into account also helps in assessing conventional TEM examinations. Interface profiles can only be accurately measured in a single projection if either the roughness is very small or the projected sample thickness is thinner than the correlation length. Obtaining sample thicknesses below the correlation length can be very challenging, especially if the preparation needs to be site-specific which highlights the advantage of this tomographic analysis.

It should also be noted that the creation of reliable isosurfaces was not possible for the Al_{0.25}Ga_{0.75}As/GaAs interfaces due to the low HAADF contrast. The precision of the isosurfaces depends on the intensity gradient at the interface. The larger the gradient, the less affected is the position of the isosurface by noise. Consequently, the noise needs to be always significantly smaller than the expected change of intensity at the interface. This can be achieved, for example, by increasing the dwell time of the scan or adapting the camera length for different acceptance angles of the HAADF mode.

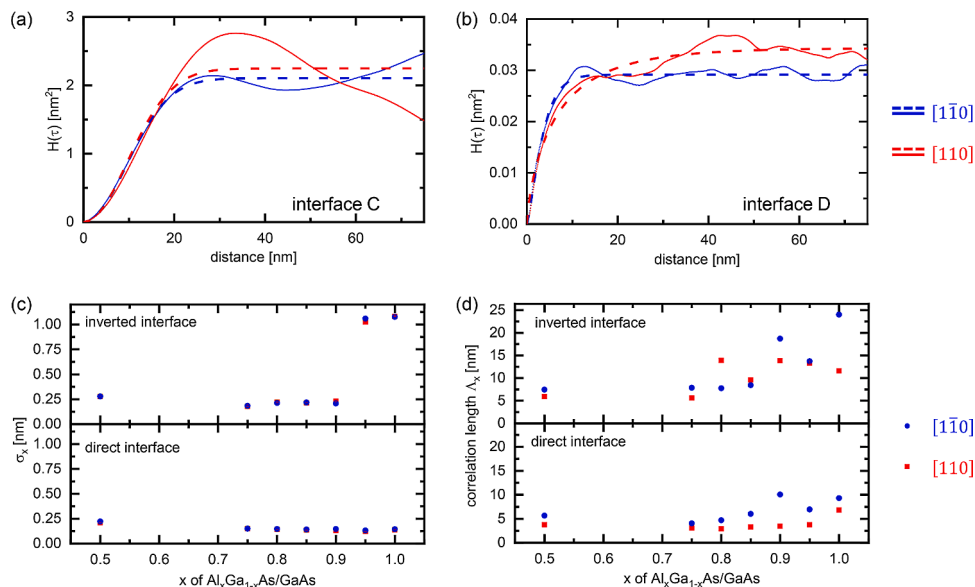


Fig. 7. Height-height correlation function of (a) interface C and (b) interface D along the $[110]$ and $[\bar{1}\bar{1}0]$ direction, respectively. The fit parameter (c) σ_x and (d) Λ_x of the HHCF function (cf. Eq. (4)) is plotted for all investigated interfaces along the $[110]$ and $[\bar{1}\bar{1}0]$ direction, respectively.

3.3. Analysis of the chemical intermixing using electron tomography

In a final step, electron tomography was used to determine the chemical intermixing at each interface position in order to obtain a comprehensive picture of the 3D structural interface property. As schematically shown in Fig. 8a, any III-V interface has a gradient in composition, and hence several isoconcentration-surfaces at different voxel intensities can be created. Accordingly, the height differences of isosurfaces of the same interface corresponding to different concentration values are used to evaluate changes in the interface width. Here, isosurfaces corresponding to 30% and 70% of the total compositional difference were generated and then rasterized as shown schematically in Fig. 8b. Subsequently, the topographic height maps of the 30%-isosurfaces were subtracted from the height maps of the 70%-isosurfaces. As a result, height-difference-maps are obtained, which spatially measure the interface distance $L_{30\%-70\%}$. On the other hand, the interface width W is typically defined in the literature by the distance at which the concentration changes from 10% to 90% of the total difference. These specific isosurfaces were not created due to the larger influence of noise on isosurfaces corresponding to these compositions. Instead, a sigmoidal profile of the concentration change across the interface was assumed so that the width $L_{30\%-70\%}$ can be extrapolated to the interface width W by using the resulting factor 2.6. The spatially resolved interface width maps of interface A, B, C, and D are depicted in Fig. 8c showing a random distribution of the spatial change of the interface width. A strong spatial variation of the chemical widths for interfaces A and C can be recognized, as it has already been mapped for the case of the RMS roughnesses (cf. Fig. 6a). Furthermore, the maps reveal higher average interface widths \bar{W} for the inverted interfaces A and C, i.e., 7.3 nm and 3.9 nm, compared to the direct interfaces, i.e., about 3 nm, for the direct interfaces. The magnitude of the variations measured by the standard deviation of the width within the full area of the maps is significantly larger for the inverted (1.5 nm and 1.1 nm) compared to the direct interfaces (0.5 nm). These results also emphasize very clearly the strength of the electron tomography interface characterization in comparison to

conventional TEM, in particular for interfaces with large variations in the physical and/or chemical width.

4. Conclusion

In conclusion, it was demonstrated that a comprehensive determination of interface properties can be achieved using electron tomography based on HAADF STEM. For this purpose, a method was developed to extract topographic height maps and interface width maps using the 3D tomographic reconstruction of an (Al,Ga)As/GaAs heterostructure and exploiting isosurfaces corresponding to different Al concentrations. This method allows the quantitative 3D characterization of interfaces by determining the RMS values and lateral correlation lengths as well as maps of the interface width W . The strength of this methodology lies in the fact that all important interface characteristics can be extracted at once and that interfacial anisotropies can be revealed due to the spatially resolved maps. Depending on the sample volume to be investigated, it is feasible to reconstruct interfaces on different length scales up to atomic resolution. In addition, due to the FIB target preparation, the analysis is position-dependent with high spatial resolution and thus allows the investigation of specific regions of a sample.

The approach using electron tomography based on HAADF competes well with other tomographic approaches such as atom probe tomography or EDX tomography. Whereas atom probe tomography has excellent chemical sensitivity and in-depth resolutions below 0.1 nm, the lateral resolution is worse with up to 1 nm [35]. The isotropic resolution of electron tomography may therefore be advantageous for the analysis of highly 3D interfaces. In EDX tomography, significant longer acquisition times are necessary to obtain a sufficient signal-to-noise ratio (x-ray counts), allowing a quantitative interface mapping. Typically higher tilt steps and smaller scan arrays are chosen for compensation, which worsens the spatial resolution compared to electron tomography [36]. However, EDX tomography becomes particularly useful in terms of high chemical resolution, especially if the HAADF contrasts between similar materials are insufficient or if the sample contains unknown elements,

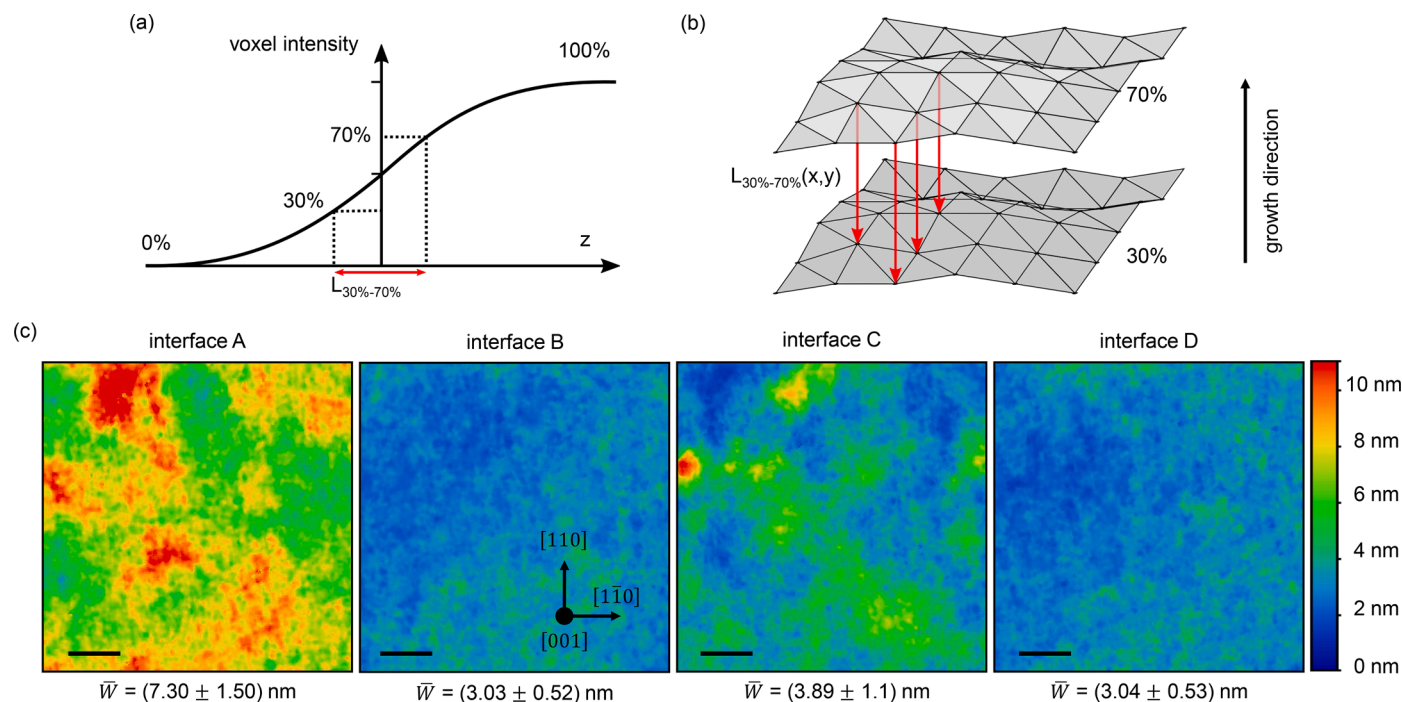


Fig. 8. Creation of interface width maps. (a) Scheme of the concentration (voxel intensity) gradient at an interface. (b) Scheme showing the spatially resolved determination of the interface width using two isosurfaces. (c) Interface width maps of the upper four interfaces. The mean interface width \bar{W} as well as the standard deviation is given for each interface. The scale bar corresponds to 20 nm.

which is less problematic for III-V heterostructures.

In general, one can state that the presented technique can be transferred to other material combinations as long as a sufficient high chemical sensitive contrast is available to allow the formation of iso-surfaces in the 3D reconstruction. Consequently, this method can be applied to investigate buried interfaces of other III-V heterostructures such as (Al,Ga)N/GaN or (In,Ga)N/GaN systems where the knowledge about the interface roughness is crucial as it is the dominant source for scattering influencing the carrier mobility.

Funding

This work was partially supported by the European Union and the state of Berlin within the frame of the European Regional Development Fund (ERDF), project number 2016011843.

Declaration of Competing Interest

The authors declare that they have no known competing financial interests or personal relationships that could have appeared to influence the work reported in this paper.

Acknowledgments

The authors are particularly grateful to M. Matzeck for the FIB preparations and acknowledge S. Fölsch for the critical reading of this manuscript.

References

- [1] H. Sakaki, T. Noda, K. Hirakawa, M. Tanaka, T. Matsusue, Interface roughness scattering in GaAs/AlAs quantum wells, *Appl. Phys. Lett.* 51 (1987) 1934–1936, <https://doi.org/10.1063/1.98305>.
- [2] T. Grange, S. Mukherjee, G. Capellini, M. Montanari, L. Persichetti, L. Di Gaspare, S. Birner, A. Attiaoui, O. Moutanabbir, M. Virgilio, M. De Seta, Atomic-Scale Insights into Semiconductor Heterostructures: from Experimental Three-Dimensional Analysis of the Interface to a Generalized Theory of Interfacial Roughness Scattering, *Phys. Rev. Applied.* 13 (2020), 044062, <https://doi.org/10.1103/PhysRevApplied.13.044062>.
- [3] A. Trampert, J.-M. Chauveau, K.H. Ploog, E. Tournié, A. Guzmán, Correlation between interface structure and light emission at 1.3–1.55 μm of (Ga,In)(N,As) diluted nitride heterostructures on GaAs substrates, *Journal of Vacuum Science & Technology B: Microelectronics and Nanometer Structures Processing, Measurement, and Phenomena* 22 (2004) 2195–2200, <https://doi.org/10.1116/1.1775197>.
- [4] H. Kroemer, Nobel Lecture: quasidelectric fields and band offsets: teaching electrons new tricks, *Rev. Mod. Phys.* 73 (2001) 783–793, <https://doi.org/10.1103/RevModPhys.73.783>.
- [5] M.J. Hÿtch, M.G. Walls, J.-P. Chevalier, Measurement of roughness and diffuseness of interfaces, *Ultramicroscopy* 83 (2000) 217–225, [https://doi.org/10.1016/S0304-3991\(00\)00016-4](https://doi.org/10.1016/S0304-3991(00)00016-4).
- [6] S.K. Sinha, E.B. Sirota, S. Garoff, H.B. Stanley, X-ray and neutron scattering from rough surfaces, *Phys. Rev. B* 38 (1988) 2297–2311, <https://doi.org/10.1103/PhysRevB.38.2297>.
- [7] R.M. Feenstra, D.A. Collins, D.Z.-Y. Ting, M.W. Wang, T.C. McGill, Scanning tunneling microscopy of InAs/GaSb superlattices: subbands, interface roughness, and interface asymmetry, *Journal of Vacuum Science & Technology B: Microelectronics and Nanometer Structures Processing, Measurement, and Phenomena* 12 (1994) 2592–2597, <https://doi.org/10.1116/1.587215>.
- [8] E. Luna, A. Trampert, J. Lu, T. Aoki, Y.-H. Zhang, M.R. McCartney, D.J. Smith, Strategies for Analyzing Noncommon-Atom Heterovalent Interfaces: the Case of CdTe-on-InSb, *Adv. Mater. Interfaces* 7 (2020), 1901658, <https://doi.org/10.1002/admi.201901658>.
- [9] S.M. Goodnick, D.K. Ferry, C.W. Wilmsen, Z. Liliental, D. Fathy, O.L. Krivanek, Surface roughness at the Si(100)-SiO₂ interface, *Phys. Rev. B* 32 (1985) 8171–8186, <https://doi.org/10.1103/PhysRevB.32.8171>.
- [10] S. Mukherjee, A. Attiaoui, M. Bauer, O. Moutanabbir, 3D Atomic Mapping of Interfacial Roughness and Its Spatial Correlation Length in Sub-10 nm Superlattices, *ACS Appl. Mater. Interfaces* 12 (2020) 1728–1736, <https://doi.org/10.1021/acsaami.9b13802>.
- [11] O. Dyck, D.N. Leonard, L.F. Edge, C.A. Jackson, E.J. Pritchett, P.W. Deelman, J. D. Poplawsky, Accurate Quantification of Si/SiGe Interface Profiles via Atom Probe Tomography, *Adv. Mater. Interfaces* 4 (2017), 1700622, <https://doi.org/10.1002/admi.201700622>.
- [12] X.Y. Zhong, B. Kabius, D.K. Schreiber, J.A. Eastman, D.D. Fong, A.K. Petford-Long, Three-dimensional quantitative chemical roughness of buried ZrO₂/In₂O₃ interfaces via energy-filtered electron tomography, *Appl. Phys. Lett.* 100 (2012), 101604, <https://doi.org/10.1063/1.3690861>.
- [13] M. Hayashida, S. Ogawa, M. Malac, Tomographic measurement of buried interface roughness, *Journal of Vacuum Science & Technology B, Nanotechnology and Microelectronics: Materials, Processing, Measurement, and Phenomena* 33 (2015), 040605, <https://doi.org/10.1116/1.4926975>.
- [14] S.J. Pennycook, Z-Contrast Transmission Electron Microscopy: direct Atomic Imaging of Materials, *Annu. Rev. Mater. Sci.* 22 (1992) 171–195, <https://doi.org/10.1146/annurev.ms.22.080192.001131>.
- [15] E. Luna, Á. Guzmán, A. Trampert, G. Álvarez, Critical Role of Two-Dimensional Island-Mediated Growth on the Formation of Semiconductor Heterointerfaces, *Phys. Rev. Lett.* 109 (2012), 126101, <https://doi.org/10.1103/PhysRevLett.109.126101>.
- [16] L.A. Giannuzzi, F.A. Stevie, A review of focused ion beam milling techniques for TEM specimen preparation, *Micron* 30 (1999) 197–204, [https://doi.org/10.1016/S0968-4328\(99\)00005-0](https://doi.org/10.1016/S0968-4328(99)00005-0).
- [17] J. Hernández-Saz, M. Herrera, S.I. Molina, A methodology for the fabrication by FIB of needle-shape specimens around sub-surface features at the nanometre scale, *Micron* 43 (2012) 643–650, <https://doi.org/10.1016/j.MICRON.2011.11.011>.
- [18] M. Niehle, A. Trampert, Electron tomography on nanopores embedded in epitaxial GaSb thin films, *Micron* 73 (2015) 54–62, <https://doi.org/10.1016/j.micron.2015.03.010>.
- [19] L. Nicolai, Ž. Gačević, E. Calleja, A. Trampert, Electron Tomography of Pencil-Shaped GaN/(In,Ga)N Core-Shell Nanowires, *Nanoscale Res. Lett.* 14 (2019) 232, <https://doi.org/10.1186/s11671-019-3072-1>.
- [20] P.A. Midgley, M. Weyland, 3D electron microscopy in the physical sciences: the development of Z-contrast and EFTEM tomography, *Ultramicroscopy* 96 (2003) 413–431, [https://doi.org/10.1016/S0304-3991\(03\)00105-0](https://doi.org/10.1016/S0304-3991(03)00105-0).
- [21] W. Van den Broek, A. Rosenauer, B. Goris, G.T. Martinez, S. Bals, S. Van Aert, D. Van Dyck, Correction of non-linear thickness effects in HAADF STEM electron tomography, *Ultramicroscopy* 116 (2012) 8–12, <https://doi.org/10.1016/j.ultramicro.2012.03.005>.
- [22] Z. Saghì, X. Xu, G. Möbus, Electron tomography of regularly shaped nanostructures under non-linear image acquisition, *J. Microsc.* 232 (2008) 186–195, <https://doi.org/10.1111/j.1365-2818.2008.02084.x>.
- [23] R.A. Crowther, D.J. DeRosier, A. Klug, The reconstruction of a three-dimensional structure from projections and its application to electron microscopy, *Proceedings of the Royal Society A* 317 (1970) 319–340, <https://doi.org/10.1098/rspa.1970.0119>.
- [24] J.M. Cowley, Y. Huang, De-channelling contrast in annular dark-field STEM, *Ultramicroscopy* 40 (1992) 171–180, [https://doi.org/10.1016/0304-3991\(92\)90058-R](https://doi.org/10.1016/0304-3991(92)90058-R).
- [25] Z. Yu, D.A. Muller, J. Silcox, Effects of specimen tilt in ADF-STEM imaging of a-Si/c-Si interfaces, *Ultramicroscopy* 108 (2008) 494–501, <https://doi.org/10.1016/j.ultramicro.2007.08.007>.
- [26] J.R. Kremer, D.N. Mastrorade, J.R. McIntosh, Computer visualization of three-dimensional image data using IMOD, *J. Struct. Biol.* 116 (1996) 71–76, <https://doi.org/10.1006/jsbi.1996.0013>.
- [27] W. van Aarle, W.J. Palenstijn, J. De Beenhouwer, T. Altantzis, S. Bals, K. J. Batenburg, J. Sijbers, The ASTRA Toolbox: a platform for advanced algorithm development in electron tomography, *Ultramicroscopy* 157 (2015) 35–47, <https://doi.org/10.1016/j.ULTRAMIC.2015.05.002>.
- [28] W. van Aarle, W.J. Palenstijn, J. Cant, E. Janssens, F. Bleichrodt, A. Dabrovolski, J. De Beenhouwer, K. Joost Batenburg, J. Sijbers, Fast and flexible X-ray tomography using the ASTRA toolbox, *Opt. Express* 24 (2016) 25129, <https://doi.org/10.1364/OE.24.025129>.
- [29] A. Buades, B. Coll, J.M. Morel, A Review of Image Denoising Algorithms, with a New One, *Multiscale Model. Simul.* 4 (2005) 490–530, <https://doi.org/10.1137/040616024>.
- [30] D. Nečas, P. Klapetek, Gwyddion: an open-source software for SPM data analysis, *Open Physics* 10 (2012) 181–188, <https://doi.org/10.2478/s11534-011-0096-2>.
- [31] D. Bimberg, D. Mars, J.N. Miller, R. Bauer, D. Oertel, J. Christen, Kinetics of island formation at the interfaces of AlGaAs/GaAs/AlGaAs quantum wells upon growth interruption, *Superlattices Microstruct.* 3 (1987) 79–82, [https://doi.org/10.1016/0749-6036\(87\)90182-0](https://doi.org/10.1016/0749-6036(87)90182-0).
- [32] D.E. Savage, J. Kleiner, N. Schimke, Y.-H. Phang, T. Jankowski, J. Jacobs, R. Kariotis, M.G. Lagally, Determination of roughness correlations in multilayer films for x-ray mirrors, *J. Appl. Phys.* 69 (1991) 1411–1424, <https://doi.org/10.1063/1.347281>.
- [33] T. Salditt, T.H. Metzger, J. Peisl, B. Reinker, M. Moske, K. Samwer, Determination of the Height-Height Correlation Function of Rough Surfaces from Diffuse X-Ray Scattering, *EPL* 32 (1995) 331–336, <https://doi.org/10.1209/0295-5075/32/4/008>.
- [34] S. Labat, C. Guichet, O. Thomas, B. Gilles, A. Marty, Microstructural analysis of Au/Ni multilayers interfaces by SAXS and STM, *Appl. Surf. Sci.* 188 (2002) 182–187, [https://doi.org/10.1016/S0169-4332\(01\)00739-5](https://doi.org/10.1016/S0169-4332(01)00739-5).
- [35] B. Gault, M.P. Moody, F.D. Geuser, A.L. Fontaine, L.T. Stephenson, D. Haley, S. P. Ringer, Spatial Resolution in Atom Probe Tomography, *Microsc. Microanal.* 16 (2010) 99–110, <https://doi.org/10.1017/S1431927609991267>.
- [36] Z. Saghì, X. Xu, Y. Peng, B. Inkson, G. Möbus, Three-dimensional chemical analysis of tungsten probes by energy dispersive x-ray nanotomography, *Appl. Phys. Lett.* 91 (2007), 251906, <https://doi.org/10.1063/1.2826273>.